Polarimetric prospects of a new hard X-soft gamma-ray space mission for next decades

M. Moita*, L. Ferro and F. Frontera
Dept. of Physics and Earth Science,
University of Ferrara, Ferrara, Italy
**E-mail: mmoita@fe.infn.it*

E. Caroli, E. Virgilli and J. B. Stephen
OAS of Bologna INAF Bologna,
Bologna, Italy

R. M. Curado da Silva and M. Maia
LIP-Laboratório de Instrumentação e Física Experimental de Partículas,
Coimbra, Portugal

S. del Sordo
IASF-Palermo INAF Palermo,
Palermo, Italy

The measurement of the polarization of the high-energy photons from cosmic sources has now become a key observational parameter for understanding the emission mechanisms and the geometry of the active regions involved. Therefore, a mandatory requirement for new instrumentation in this energy regime will provide high sensitivity for polarimetric measurements associated with spectroscopy and imaging.

In this perspective, the Advanced Surveyor of Transient Events and Nuclear Astrophysics (ASTENA) mission, which includes two main instruments: the Wide field monitor (WFM-IS), with a large effective area and a wide energy passband (2 keV – 20 MeV); and the Narrow Field Telescope (NFT), with a broad energy passband (50–600 keV) with focusing capabilities based on the use of an advanced Laue lens; will both provide high sensitivity for polarimetric measurements. Furthermore, both instruments will include spectometers with a good 3D spatial resolution allowing to perform 3D Compton polarimetry, increasing the possibilities to optimize the event selection. Herein, we report on the results of a Monte Carlo study devoted to optimize the configuration of both instruments, in particular, the modulation factor (Q), the events detection efficiency (Eff) and the Minimum Detectable Polarization (MDP).

Keywords: Polarimetry, Gamma-ray detectors, Space instrumentation, Compton scattering.

1. Introduction

Polarimetry of high-energy sources is a key observational parameter for a better understanding of the emission mechanisms and geometry of a wide number of cosmic objects and events such as GRBs, pulsars, binary black holes and active galactic nuclei, whose emissions are expected to be polarized. The field of hard

X-ray polarimetry has been quite active in the last two decades: missions such as INTEGRAL, AstroSat and POLAR have provided some important scientific inputs in understanding emission mechanism and geometry in X-ray pulsars,[1–3] magnetic field structure in Pulsar Wind Nebula (PWN),[1,4] disk-jet interplay in black hole X-ray binaries (XRBs)[5,6] and hard X-ray emission mechanism in GRB prompt emission.[7–9] Though these results are marred with large uncertainties and a firm conclusion is not possible, most of these findings are extremely interesting as they pose new challenges to the existing theories. One interesting and common feature in all these measurements is a systematic increase in polarization within the hard X-ray band which makes this energy regime extremely promising for polarimetry experiments.[10]

As a part of the European project AHEAD (integrated Activities in the High Energy Astrophysics Domain), a new concept of high energy mission named ASTENA (Advanced Surveyor of Transient Events and Nuclear Astrophysics) has been proposed and accepted for feasibility and performance study.[11] In the current AHEAD 2020 project, which is a continuation of AHEAD, we deepen the feasibility study of ASTENA and increase our knowledge on the potential performances of the instruments on board concerning spectral, imaging and, particularly in this context, polarization capabilities. In this work we present the results of a study that aims to reliably and realistically evaluate the performance in terms of polarimetry that can be achieved with the ASTENA and to optimize the design of the detection units to achieve this aim taking into account the requirements.

2. ASTENA

The ASTENA configuration is described in,[12] and it is shown in Fig. 1. Its main properties are summarized in Table 1. The instrumentation on board consists of a Wide Field Monitor–Imaging Spectrometer (WFM-IS) with a 2 keV–20 MeV passband, and a Narrow Field Telescope (NFT) with a 50–600 keV passband.

Table 1. Summary of the main properties of the WFM-IS and of the NFT on board ASTENA.

	WFM-IS	NFT
Energy pass-band	2 keV – 20 MeV	50 – 600 keV
Total useful area$^{(a)}$	$\sim$ 5800 cm^2 ($<$ 30 keV) $\sim$ 6700 cm^2 (30–150 keV) $\sim$ 13800 cm^2 ($>$200 keV)	7 m^2 (projected)
Field of View	2 sr	4 arcmin
Angular resolution	6 arcmin	$\sim$ 30 arcsec HPD
Point source localization accuracy	1 arcmin	$<$ 10 arcsec
3σ, **Continuum Sensitivity** (ph/cm^2 s keV)	1×10^{-4} (10 s, 30–150 keV)	1.2×10^{-9} (10^5 s, 225–375 keV)
3σ, 10^5 s **Line sensitivity** (ph/cm^2 s)	-	5×10^{-7} (178 keV)

Note: $^{\rm a}$Total geometric area through the mask or collimator.

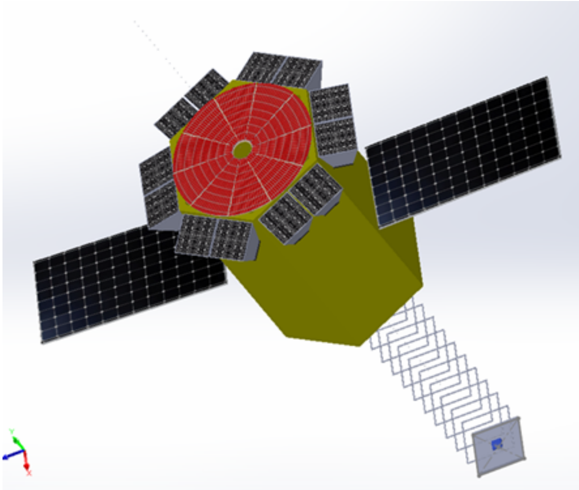

Fig. 1. The ASTENA satellite in inflight configuration. The WFM/S modules surround the NFT Laue lens (front), while its focal plane is positioned 20 m apart by a booming structure (back).

The NFT is a Laue lens focusing telescope with a 3 m diameter and 20 m focal length, composed by a large number of crystal tiles in transmission configuration, that are disposed in such a way that they concentrate the incident radiation onto a common focal spot.[13] The lens proposed for the NFT is made of ∼19500 bent crystal tiles of Si(111) and Ge(111), with 40 m curvature radius (within 5% uncertainty). The crystal tiles have a 30×10 mm^2 cross section, and an optimized thickness vs. energy for maximizing the diffraction efficiency, with the condition of a maximum thickness of 5 mm. The crystals are disposed on 43 rings, with an outermost ring radius of 149 cm and an innermost of 18 cm, ensuring an energy passband of 50 keV (outermost rings) to 600 keV (innermost rings). Current Monte Carlo simulations, ray-trace analyses and laboratory experiments evaluated that an angular resolution of 0.5 arcmin can be achieved, with a useful FOV of approximately 4 arcmin.[14]

Concerning the NFT focal plane detector, the adopted configuration consists of 4 layers of drift strip detectors of CdZnTe,[15] each layer with a cross section a 80×80 mm^2 and a thickness of 20 mm. This configuration will ensure a detection efficiency higher than 80% in the entire energy band of the NFT, a spectroscopy response of 1% @ 511 keV and fine spatial resolution (0.2–0.3 mm) in three dimensions,[16] allowing the correct sampling of the Point Spread Function (PSF) of the lens, that is of the order of a few mm^2. Thanks to the unprecedented sensitivity that can be achieved with the Laue lens focusing technique and the high segmentation level the focal plane detector, NFT is expected to provide fine polarization measurements.

The WFM-IS consists of an array of 12 units, two units on each side of the hexagon surrounding the NFT, accommodated as shown in Fig. 1. All the units are offset by 15 deg with respect to the axis of the NFT. Each WFM-IS unit consists of a 40 × 40 array of detection elements, each made of a scintillator bar (CsI(TI) or similar) 5 cm long, with an hexagonal cross section of about 75 mm^2, viewed by two Silicon Drift Detectors (SDD) 0.4 mm thick, one on the top (side of entrance of the celestial photons) and other on the bottom. The functioning principle of this detector is similar to that adopted for the X-Gamma-ray Imaging Spectrometer (XGIS) aboard the THESEUS mission concept.[17] It has the great advantage of a very broad passband (2 keV–20 MeV), a 3-D position sensitivity to energy losses in the scintillator bars and a very low intrinsic background. The hexagonal cross section of the bars, which allows us to obtain a low geometric systematic effect in the polarization measurements, associated with the 3D position sensitivity of the detector makes the WFM-IS suitable for fine polarization measurements.[11]

3. Compton Polarimetry with ASTENA

In the hard X- and soft γ-rays regime the measurement of the polarization status of a photon beam rely on the Compton scattering mechanism. The detectors on-board ASTENA provide the segmentation needed to offer an efficient method to measure the linear polarisation of incoming photons using Compton scattering because, with a coincidence event logic, each element/pixel can act at the same time both as a scattering element and as a detection unit allowing to record the pairs of events that provide polarimetric information: one is the Compton scattering of the incoming photon, the other is the interaction by Compton or photoelectric effect of the secondary photon.[10]

The cross-section of a hard X-ray photon to interact with a free electron is given by the Compton scattering cross-section described by the Klein–Nishina equation[18]:

$$\frac{d\sigma}{d\Omega} = \frac{r_0^2 \varepsilon^2}{2} \left(\frac{1}{\varepsilon} + \varepsilon - 2 \sin^2 \theta \cos^2 \varphi \right) \tag{1}$$

where r_0^2 is the classic electron radius, $\varepsilon = E'/E$ the ratio between the energy of the scattered photon and the energy of the incoming photon, θ is the scattering angle of the scattered photon measured from the direction of the incident photon, and φ is the azimuth scattering angle with respect to the electric vector of the incident photon. On a segmented detector the distribution of the azimuthal angle measured on a large sample of data has a sinusoidal behavior with period π

$$N(\phi) = a_0(1 + a_1 \cos(2(\phi - a_2 + \pi/2))) \tag{2}$$

where a_0 is the normalization constant, $Q = a_1$ the modulation factor, and $P = a_2$ the polarization angle which are obtained from a fit to the data. This distribution is the called "modulation curve", which is built dividing the scattering map on a fixed number of angular sectors, covering 360°, and integrating the counts inside each angular sector. The aperture of the angular sectors should be chosen taking into account the discretization level of the detector (i.e., the pixel dimensions) and the counts statistics. Because of the segmented nature of the detector, the integration of count inside a defined angular sector should take into account effects due to pixels that lie across their borders. Methods to account for these pixels are, for example, that of distributing uniformly the pixel counts proportionally to the area of the pixel intercepted by two adjacent angular sectors. For the analyses performed the number of bins of the azimuthal distribution was optimized for each instrument since it affects the shape of the modulation curve.

In the characterization of a polarimeter it is important to describe its response not only to polarized, but also to unpolarized signals. For a perfectly uniform and symmetric instrument the modulation curve from a 0% polarized signal should be totally flat. However, the detector geometry introduces an asymmetry that is important to correct the signal from this component. We correct the measured modulation curve from the instrument response to a unpolarized signal by applying the following expression for each angle bin:

$$N_{corr}(\phi) = \frac{N_p(\phi)}{N_{np}(\phi)} N_{np}^{max} \tag{3}$$

where $N_{corr}(\phi)$ is the corrected azimuthal distribution, $N_p(\phi)$ is the polarized azimuthal distribution, $N_{np}(\phi)$ the non polarized modulation azimuthal distribution, and N_{np}^{max} the maximum of the non polarized azimuthal distribution. In practice, the systematic uncertainty in the polarization measurement will be estimated from the results of an extensive on-ground calibration campaign of the instruments, using both polarized and unpolarized monochromatic beams of gamma rays.

The minimum detectable polarization (MDP) of an instrument for a given celestial source type is an essential parameter to estimate its polarimetric potential. For a space polarimeter in a background dominated environment, the MDP with a 99% confidence level, is given by[19]:

$$MDP = \frac{4.29}{A.\epsilon.S_F.Q_{100}} \sqrt{\frac{A.\epsilon.S_f + B}{T}} \tag{4}$$

where, A is the effective area, ϵ is the events' efficiency, S_F is the source flux over the selected energy band (photons cm^{-2} s^{-1}), B is the background noise count rate (counts/s), T is the observation time (s) and Q_{100} is the polarimetric modulation factor for a 100% polarized source.

High polarimetric performance for hard X/soft γ-rays can be achieved fulfilling the following requirements: high scattering efficiency, fine spatial resolution, and fine spectroscopy. These characteristics allow a large flexibility in scattered events selection, and therefore several event filter can be implemented to optimize the modulation factor and the event efficiency, and consequently improve the MDP.

4. Polarimetric Analyses for a Monochromatic Source

4.1. *NFT*

In order to fulfil the requirements on the ASTENA NFT, and following the knowhow acquired by both experiments on CdTe/CZT detectors used as scattering polarimeter and development on 3D CZT spectrometers,[20] a simple model of the NFT focal plane has been implemented using MEGALib tools.[21] Using the MEGAlib/Geomega package, we implement a numerical model made of a stack of 4 thick layers of CZT separated by a layer (10 mm thick) of a PCB type mixture passive material, representative of the read-out front-end electronics board (Fig. 2). Each CZT layer is 20 mm thick and 80 mm × 80 mm wide. The CZT layers were divided in voxels with dimensions 0.25 x 0.25 x 0.25 mm^3 each. The spectroscopic response of the detector is simply modeled by a relationship derived from measurements on CZT drift strips spectrometers.[22] In all the performed simulation runs, we set the low energy threshold to 5 keV, that is a reasonable value at room temperature as demonstrated by the same experimental results.

The Laue lens configuration will impinge an almost monochromatic beam for each crystal ring on the detector, each one having a small inclination angle with respect to the axis of the lens, ranging from 0.4° (at the energy of 600 keV, corresponding to the inner radius) to 4.5° (at the energy of 50 keV, corresponding to the external radius). This will produce rings of photons with similar energy hitting the detector inside a PSF. We know from previous experiments that an off-axis beam introduce geometric effects on the detector that affect the modulation factor.[23] However, since the Laue lens presents a 180° symmetry, for each beam there will be a symmetric beam with opposite off-axis angle. This configuration will correct any possible systematic error due to the off-axis beam and the results will be similar as we impinge an on-axis beam on the detector. In fact, a systematic study was performed in order to validate this assumption. We evaluated the modulation factor by varying the number of pair of symmetric off-axis beams from 1 to 128, obtaining a distribution of values for the modulation factor with a standard deviation of 0.02 from the central value which is comparable with the error on the values of the modulation factor. To simulate a full Laue lens would require ∼20000 beams, each with its off-axis angle, however, by taking into account the aforementioned results, we decided to use instead a Gaussian cone shape beam, 20 m from the detector, which produce a Gaussian shape PSF with a FWHM of 0.15 cm on the top of the detector. This will simplify the simulation code and speed up the simulations without compromising the result.

To ensure the quality of the selected events we perform a check by Compton kinematics – by evaluating the energy of the two first interactions and the corresponding scattering angle we ensure that it corresponds to the expected values and the event can be selected as a “good event”. This also can be done for multiple interactions, by using the energy of the first interaction, the sum of the following interactions

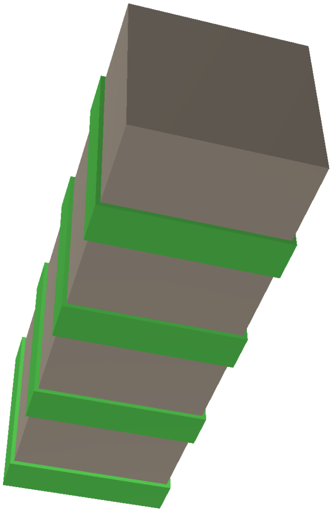

Fig. 2. Monte Carlo model of the the NFT focal plane. The gray volumes represent the segmented CZT spectrometer, while the green ones represent the readout electronics boards.

and the scattering angle from the first and second interaction. This method ensures that all the events selected are true Compton events and have polarimetric information on it. This method also removes the double events that occur in neighbour pixels. These type of events can introduce anomalies because the scattering angle is difficult to know. Since we consider the interaction in the center of pixel these types of events will be considered as a ∼90° scattering event (high polarimetric information). However, if the interactions occur near the edges of the pixels the scattering angle can be ∼0° (low polarimetric information).

Due to the focusing properties of the NFT we know that the first interaction is always inside the PSF. These allows a further correction since we only select the events which complies with this condition. This will reduce the background or any spurious events that occur in the detector.

After the selections, the scattering maps and modulation curves are drawn. To correct the systematic effects introduced by the detector geometry we also simulate an unpolarized source in the same conditions as the polarized source and we corrected the distributions with equation 3. As an example Fig. 3 presents the scattering maps obtained for a 300 keV unpolarized beam and for a 100% polarized beam with a polarization vector direction of 60°. By diving the scattering maps into 24 bins we achieved the azimuthal distributions presented in Fig. 3, below each scattering map. The corrected modulation curve is presented in Fig. 4. The corrected curve is then fitted with equation 2 to get the modulation factor and the polarization angle.

In Fig. 5 it is presented the modulation factor as function of the energy for the NFT focal plane for monochromatic beams ranging from 100 to 600 keV. These

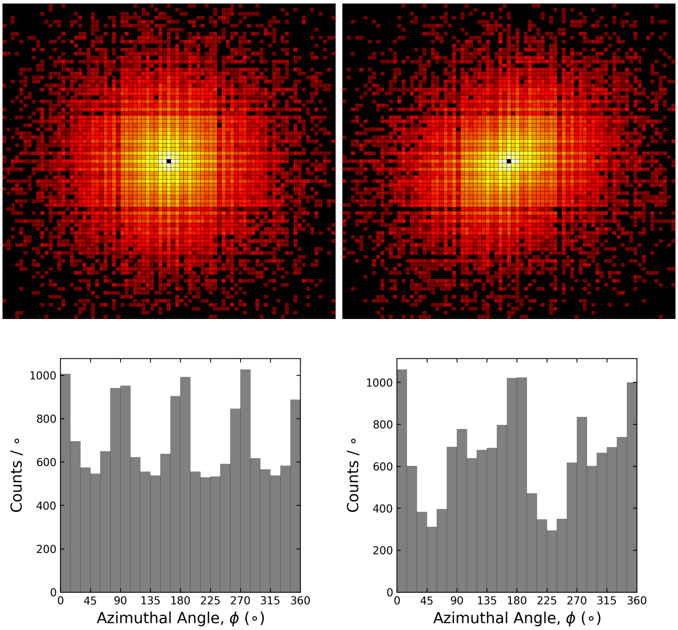

Fig. 3. Scattering maps and azimuthal distributions obtained for an unpolarized (left) and 100% polarized (right) beam. The beam energy is 300 keV and the polarization vector direction is 60° for the 100% polarized case.

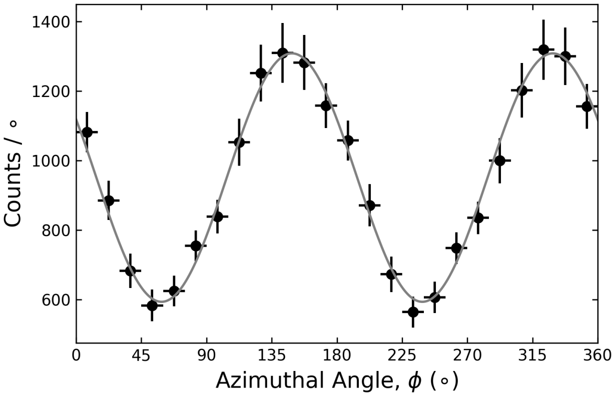

Fig. 4. Corrected modulation curve obtained when we apply the correction in Eq. (3) on the histograms of Fig. 3.

results showed that the NFT Focal Plane Detector (FPD) has potential to perform polarimetric analysis in the whole energy range presenting modulation factors >0.2. As expected, the best modulation factor is obtained at energies ∼300 keV.

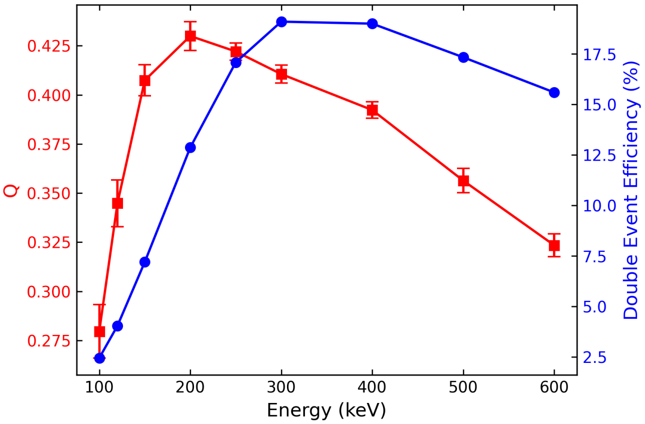

Fig. 5. NFT modulation factor and event efficiency as function of the energy.

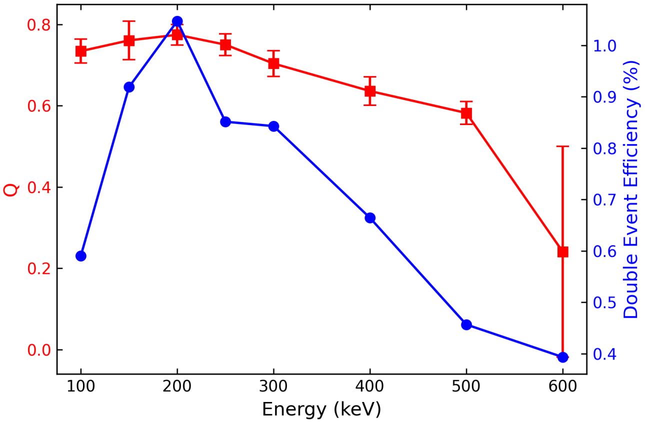

Fig. 6. NFT modulation factor and event efficiency as function of the energy for events with scattering angles of ∼90°.

The percentage of selected events shows its maximum at ∼200 keV where the Compton cross section prevails over the other interactions in the CZT.

Due to the highly segmented detector we can also select events that maximize the modulation factor like events with scattering angles ∼90° (along the detector axis). By making a selection in the Z coordinates we ensure that all the events have ∼90°. In Fig. 6 it is shown the modulation factor as a function of the energy taking account this selection. As can be seen, there is a big increase of the modulation factor when compared with the results without selection. The modulation factor reaches values near ∼0.8 for energies ∼200 keV. However the efficiency is very affected and reduced to values below ∼1%.

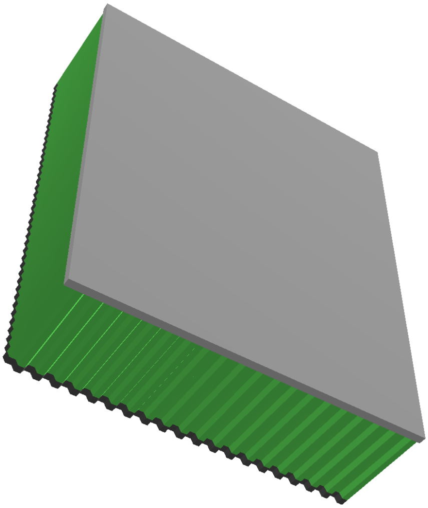

Fig. 7. A geometry sketch of the the WFM-IS unit. The green volume represent the CsI scintillators, while the gray ones represent the Si SDDs, light gray on top and dark gray on bottom.

4.2. *WFM-IS*

The Monte Carlo model of one WFM-IS unit is presented in Fig. 7. It consists of an hexagonal 40x40 array of CsI scintillators (for a total of 205 bars), with a distance between contiguous centres across hexagon flat sides of 5 mm, and a length of 50 mm. To mimic the depth resolution of the detector we segmented the bars in 10 segments of 5 mm each. On the top the detector has a linear SDD, 0.4 mm thick, and, on bottom an hexagonal single anode SDD, 0.4 mm thick, with a distance between hexagon flat sides of 5 mm. To construct the full WFM-IS we copied 12 units and placed along an hexagonal configuration, 2 units in each hexagon side, with a distance from the center (lens axis) of 1.5 m.

Since the WFM-IS is a wide field instrument, the beam used for the simulations was a far point source. For the WFM-IS we do not know were the beam undergoes the first interaction, all the scintillating bars will be scattering and absorbing elements, so we selected the events that comply the Compton kinematics and we corrected the signal data with the unpolarized data. In Fig. 8 the scattering maps are shown for a 500 keV unpolarized and 100% polarized source.

A systematic study was performed using monochromatic sources from 125 keV to 5 MeV. Fig. 9 shows the modulation factor and efficiency obtained for one WFM-IS unit and the full WFM-IS. As can be seen, for energies below 1 MeV the modulation factor shows values >0.2, however for energies above 1 MeV the modulation factor drops drastically becoming impossible to get polarization results. The reason for this is that for energies > 1 MeV both the theoretic value of the modulation factor and the efficiency of the Compton process drop significantly.[10] When comparing

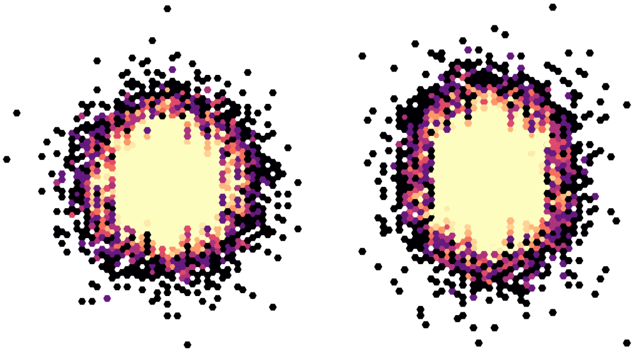

Fig. 8. Scattering maps obtained for a 500 keV unpolarized (left) and 100% polarized (right) beam with the WFM-IS unit. The polarization vector direction is 0° for the 100% polarized case.

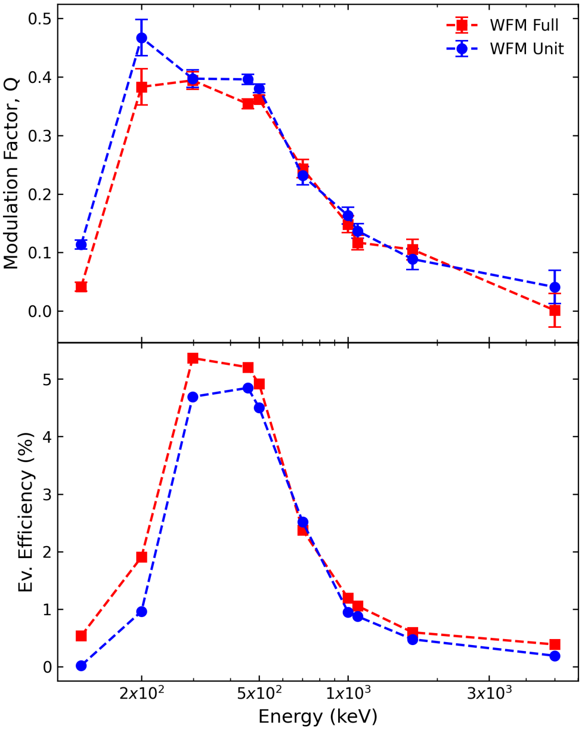

Fig. 9. Modulation factor (top) and event efficiency (bottom) as function of the energy for one WFM-IS unit and for the full WFM-IS.

the results for one WFM-IS unit and for the full WFM-IS the results of the modulation factor are similar, however the event efficiency increases when using the full WFM-IS.

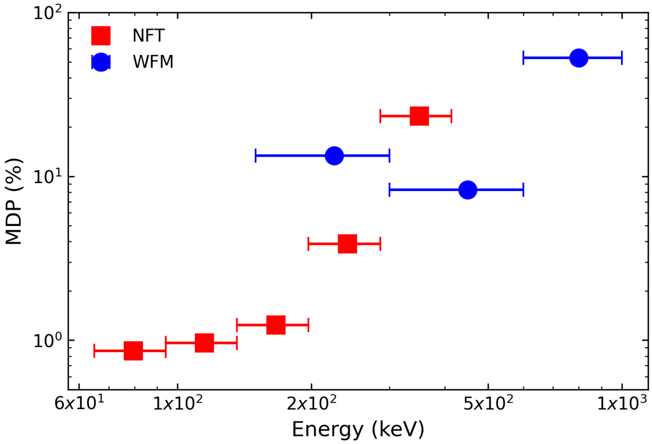

Fig. 10. Minimum detectable polarization (MDP) versus energy for a 100 mCrab source when observing with NFT and WFM-IS for 100 ks.

5. Polarimetric Sensitivity of ASTENA

In order to estimate the potential MDP of the ASTENA mission in a LEO (low Earth orbit) when observing a Crab type source, we simulated a source with a power law spectrum (normalization at 1 keV: 10.74 photons $\text{keV}^{-1}\ \text{s}^{-2}\ \text{cm}^{-2}$; photon index: 2.17) for each instrument individually and obtained the modulation factor and event efficiency. The simulated energy range was in accordance with the instrument energy passband: for the NFT 65 – 600 keV; and for the WFM-IS 150 keV – 1 MeV. As before, we simulated an on-axis Gaussian cone beam to mimic the 1.5 mm diameter of the Lens PSF for the NFT and a on-axis far source for the WFM-IS.

The background components were modeled in detail also using the MEGAlib environment tools for both NFT and WFM-IS using the works.[24–28] Background simulations were performed for both instruments individually and, to determine the real background for polarimetric analyses, we also performed the same selection process as the data. First we checked the events by Compton kinematics and, for the NFT data, we check if the first interaction is inside the PSF.

The effective area of the NFT was computed analytically as the product of the geometrical area of the instrument and the reflection efficiency of the lens[14] times the effective area for the WFM-IS was estimated using MEGAlib simulations.

The calculated MDP as a function of the energy when observing a 100 mCrab source for 100 ks is presented in Fig. 10. As can be seen, for energies < 200 keV the NFT presents MDP values $\sim 1\%$. However, above that energy it starts to substantially degrade because of the decrease of effective area of the Laue lens. For energies above 300 keV the WFM-IS presents a better MDP than the NFT meaning that the instruments can complement each other in energy bands.

6. Conclusions

In the next missions for medium energy astrophysics, polarimetry will be a fundamental requirement for the solution of important scientific problems related to the nature and geometry of the high energy cosmic sources emission. The ASTENA mission, under study as part of the European project AHEAD 2020, thanks to the high efficient, fine spectral resolution and high segmentation of the detectors onboard will be able to make polarimetry a standard way of observation by definitively opening this observation window also in the field of hard X- and soft γ-rays.

In this work we presented the results of an ongoing study which aims at a reliable and realistic evaluation of the performance in terms of polarimetry achievable with ASTENA, and obtain information for optimizing the design of the detection systems. The results show that the NFT will be able to achieve unprecedented polarametric capabilities for energies between 60 - 300 keV, while the WFM-IS will be capable to provide polarimetric measurements up to 1 MeV. ASTENA polarimetric performances show that such instruments hold the potential to address gamma-ray polarimetry with high sensitivity and contribute to expanding this new astrophysics knowledge window.

Acknowledgements

This work has been partially supported with the financial contribution from the ASI-INAF agreement n. 2017-14-H.0 “Studi per future missioni scientifiche”, the ASI-INAF agreement n. 2018-10-H.1-2020 “HERMES Technologic Pathfinder”, and the AHEAD EU Horizon 2020 project (Integrated Activities in the High Energy Astrophysics Domain), grant agreement n. 871158.

References

1. S. V. Vadawale, Chattopadhyay *et al.*, Phase-resolved X-ray polarimetry of the Crab pulsar with the AstroSat CZT Imager, *Nature Astronomy* **2**, p. 50–55 (2018).
2. M. Forot, P. Laurent, I. A. Grenier, C. Gouiffès and F. Lebrun, Polarization of the crab pulsar and nebula as observed by the INTEGRAL/IBIS telescope, *The Astrophysical Journal* **688**, L29 (nov 2008).
3. E. Jourdain and J.-P. Roques, 2003–2018 monitoring of the crab nebula polarization in hard x-rays with INTEGRAL SPI, *The Astrophysical Journal* **882**, p. 129 (sep 2019).
4. A. J. Dean, D. J. Clark, J. B. Stephen, V. A. McBride, L. Bassani, A. Bazzano, A. J. Bird, A. B. Hill, S. E. Shaw and P. Ubertini, Polarized gamma-ray emission from the crab, *Science* **321**, 1183 (2008).
5. P. Laurent, J. Rodriguez, J. Wilms, M. Cadolle Bel, K. Pottschmidt and V. Grinberg, Polarized gamma-ray emission from the galactic black hole cygnus x-1, *Science* **332**, p. 438–439 (Mar 2011).
6. E. Jourdain, J. P. Roques, M. Chauvin and D. J. Clark, Separation of two contributions to the high energy emission of cygnus x-1: Polarization measurements with INTEGRAL SPI, *The Astrophysical Journal* **761**, p. 27 (nov 2012).

7. S.-N. Zhang, M. Kole *et al.*, Detailed polarization measurements of the prompt emission of five gamma-ray bursts, *Nature Astronomy* **3**, 258 (Mar 2019).
8. T. Chattopadhyay, S. V. Vadawale, E. Aarthy, N. P. S. Mithun, V. Chand, A. Ratheesh, R. Basak, A. R. Rao, V. Bhalerao, S. Mate, A. B., V. Sharma and D. Bhattacharya, Prompt emission polarimetry of gamma-ray bursts with the AstroSat CZT imager, *The Astrophysical Journal* **884**, p. 123 (Oct 2019).
9. D. Götz, P. Laurent, F. Lebrun, F. Daigne and Ž. Bošnjak, Variable polarization measured in the prompt emission of grb 041219a using ibis on board INTEGRAL, *The Astrophysical Journal* **695**, L208 (Apr 2009).
10. T. Chattopadhyay, Hard x-ray polarimetry – an overview of the method, science drivers and recent findings (2021).
11. F. Frontera, "understanding the origin of the positron annihilation line and the physics of the supernova explosions".
12. F. Frontera, E. Virgilli, C. Guidorzi, P. Rosati, R. Diehl, T. Siegert, C. Fryer, L. Amati, N. Auricchio, R. Campana, E. Caroli, F. Fuschino, C. Labanti, M. Orlandini, E. Pian, J. B. Stephen, S. Del Sordo, C. Budtz-Jorgensen, I. Kuvvetli, S. Brandt, R. M. C. da Silva, P. Laurent, E. Bozzo, P. Mazzali and M. D. Valle, Understanding the origin of the positron annihilation line and the physics of supernova explosions, *Experimental Astronomy* **51**, 1175 (June 2021).
13. F. Frontera and P. von Ballmoos, Laue Gamma-Ray Lenses for Space Astrophysics: Status and Prospects, *X-Ray Optics and Instrumentation, 2010. Special Issue on X-Ray Focusing: Techniques and Applications, id.215375* **2010** (2010).
14. E. Virgilli, V. Valsan, F. Frontera, E. Caroli, V. Liccardo and J. B. Stephen, Expected performances of a Laue lens made with bent crystals, *Journal of Astronomical Telescopes, Instruments, and Systems* **3**, p. 044001 (October 2017).
15. I. Kuvvetli, C. Budtz-Jørgensen, E. Caroli and N. Auricchio, CZT drift strip detectors for high energy astrophysics, *Nuclear Instruments and Methods in Physics Research A* **624**, 486 (December 2010).
16. I. Kuvvetli, C. Budtz-Jørgensen, A. Zappettini, N. Zambelli, G. Benassi, E. Kalemci, E. Caroli, J. B. Stephen and N. Auricchio, A 3D CZT high resolution detector for x- and gamma-ray astronomy, in *High Energy, Optical, and Infrared Detectors for Astronomy VI*, eds. A. D. Holland and J. Beletic (SPIE, 2014).
17. R. Campana, F. Fuschino, C. Labanti, L. Amati, S. Mereghetti, M. Fiorini, F. Frontera, G. Baldazzi, P. Bellutti and et al., The X-Gamma Imaging Spectrometer (XGIS) onboard THESEUS, *Mem. Soc. Astron. Italiana* **89**, p. 137 (2018).
18. O. Klein and Y. Nishina, Über die Streuung von Strahlung durch freie Elektronen nach der neuen relativistischen Quantendynamik von Dirac, *Zeitschrift für Physik* **52**, 853 (1929).
19. M. C. Weisskopf, E. H. Silver, H. L. Kestenbaum, K. S. Long and R. Novick, A precision measurement of the X-ray polarization of the Crab Nebula without pulsar contamination., *The Astrophysical Journal* **220**, L117 (March 1978).
20. L. Abbene *et al.*, Recent advances in the development of high-resolution 3d cadmium–zinc–telluride drift strip detectors, *Journal of Synchrotron Radiation* **27**, 1564 (2020).
21. A. Zoglauer, Megalib: Medium energy gamma-ray astronomy library.
22. I. Kuvvetli, Development of cdznte detector systems for space applications, PhD thesis, Technical University of Denmark 2003.
23. R. M. C. da Silva *et al.*, Polarimetry study with a CdZnTe focal plane detector, *IEEE Transactions on Nuclear Science* **58**, 2118 (2011).

24. T. Mizuno, T. Kamae, G. Godfrey, T. Handa, D. J. Thompson, D. Lauben, Y. Fukazawa and M. Ozaki, Cosmic-ray background flux model based on a gamma-ray large area space telescope balloon flight engineering model, *The Astrophysical Journal* **614**, p. 1113–1123 (Oct 2004).
25. M. Kole, M. Pearce and M. Muñoz Salinas, A model of the cosmic ray induced atmospheric neutron environment, *Astroparticle Physics* **62**, 230 (2015).
26. E. Churazov, S. Sazonov, R. Sunyaev and M. Revnivtsev, Earth X-ray albedo for cosmic X-ray background radiation in the 1–1000 keV band, *Monthly Notices of the Royal Astronomical Society* **385**, 719 (02 2008).
27. S. Sazonov, E. Churazov, R. Sunyaev and M. Revnivtsev, Hard X-ray emission of the Earth's atmosphere: Monte Carlo simulations, *Monthly Notices of the Royal Astronomical Society* **377**, 1726 (05 2007).
28. M. Türler, M. Chernyakova, T. J.-L. Courvoisier, P. Lubiński, A. Neronov, N. Produit and R. Walter, Integralhard x-ray spectra of the cosmic x-ray background and galactic ridge emission, *Astronomy and Astrophysics* **512**, p. A49 (Mar 2010).